Bornite (Cu₅FeS₄) nanocrystals as an ultrasmall biocompatible NIR-II contrast agent for photoacoustic imaging

Vinoin Devpaul Vincely [a], Xingjian Zhong [b,c], Kristie Huda [a], Swathi P. Katakam [a], Joshua C. Kays [b], Allison M. Dennis [c,d], Carolyn L. Bayer [a,*]

[a] *Department of Biomedical Engineering, Tulane University, 6823 St. Charles Ave, New Orleans, LA 70118, United States*
[b] *Department of Biomedical Engineering, Boston University, Boston, MA 02215, United States*
[c] *Department of Chemical Engineering, Northeastern University, 360 Huntington Ave, Boston, MA 02115, United States*
[d] *Department of Bioengineering, Northeastern University, 360 Huntington Ave, Boston, MA 02115, United States*

ARTICLE INFO

ABSTRACT

In this study, we demonstrate the potential of the bornite crystal structure (Cu_5FeS_4) of copper iron sulfide as a second near infrared (NIR-II) photoacoustic (PA) contrast agent. Bornite exhibits comparable dose-dependent biocompatibility to copper sulfide nanoparticles in a cell viability study with HepG2 cells, while exhibiting a 10-fold increase in PA amplitude. In comparison to other benchmark contrast agents at similar mass concentrations, bornite demonstrated a $10\times$ increase in PA amplitude compared to indocyanine green (ICG) and a $5\times$ increase compared to gold nanorods (AuNRs). PA signal was detectable with a light pathlength greater than 5 cm in porcine tissue phantoms at bornite concentrations where in vitro cell viability was maintained. In vivo imaging of mice vasculature resulted in a $2\times$ increase in PA amplitude compared to AuNRs. In summary, bornite is a promising NIR-II contrast agent for deep tissue PA imaging.

1. Introduction

Exogenous agents for photoacoustic (PA) imaging can improve deep tissue image contrast [1–14]. Ideal exogenous agents will have increased optical absorption in comparison to endogenous chromophores, with absorption peaks tunable to wavelengths optimal for deeper imaging. Wavelengths from the second near infrared window (NIR-II) have been used to demonstrate deeper PA imaging due to the reduced tissue attenuation and higher exposure thresholds [15–17], and multiple exogenous agents have been developed within the NIR-II window for deep tissue imaging [18–20]. Exogenous agents can be free or nano-constructs of organic dyes [8,13,21] or synthetic nanostructures [7,10, 11,22–26]. Small molecule dyes are often commercially available and readily metabolized by biological systems. Indocyanine green (ICG) has been investigated as a PA contrast agent due to its US Food and Drug Administration (FDA)-approval for human use [8,9,13]. However, many organic dyes have concentration- and environment-dependent changes in optical properties. Additionally, they are typically synthesized to have strong optical absorption in the first NIR window, making distinction from other *in vivo* sources of contrast difficult [8,13]. Many organic dyes

with high absorbance also fluoresce, leading to a loss in transfer of optical energy to vibrational energy [27]. These issues, coupled with a lack of photostability, make organic dyes unreliable for quantitative PA imaging.

Synthetic nanostructures such as plasmonic NPs have high optical extinctions due to localized surface plasmon resonance (LSPR), an oscillation of free charge carriers (electrons or holes) in the presence of an irradiating electric field [22,28]. AuNRs in particular have high, tunable, LSPR (Fig. 1) and are relatively chemically stable [1,3,28,29]. The surface properties of AuNRs can be easily modified by a variety of bioconjugation methods to target the nanoparticles to molecular cell receptors of interest [1–3,10,28,29]. However, to shift the peak LSPR to the NIR-II window, high aspect ratios (~6) are required, resulting in AuNRs with dimensions of 80–150 nm (length) by 12–25 nm (width) [2]. Multiple studies have reported the dependence of nanoparticle biocompatibility and clearance on its size [30–33]. It has been demonstrated that particles with sizes below 5 nm can be cleared renally [32, 33]. Therefore, these larger sizes can result in the accumulation of AuNRs in the reticuloendothelial system and lead to cellular dysfunction [34].

* Corresponding author.
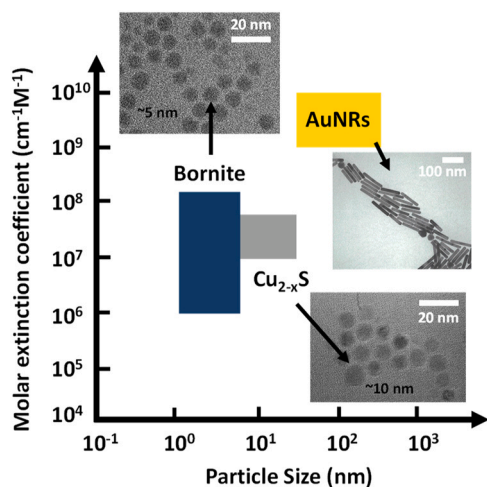*E-mail address:* carolynB@tulane.edu (C.L. Bayer).

Fig. 1. Comparison of the particle size and molar optical extinction coefficient of PAI contrast agents. The reported values include gold nanorods (yellow bar) [1–3], copper sulfide (gray bar) [4,5] and bornite (blue bar) [6]. Transmission electron microscopy images of bornite (measured), $Cu_{2-x}S$ (measured) and AuNRs (provided by manufacturer).

Plasmonic semiconductor nanocrystals (NCs) are attractive photoacoustic agents for *in vivo* imaging due to their photophysical properties [4,6,22,23,26,35,36]. Doping (intrinsic or extrinsic) of the particles increases free carrier concentration and shifts the peak LSPR from visible to mid-infrared wavelengths, without changing the shape/size of the particles; semiconductor NCs exhibit peak LSPR at longer near infrared wavelengths while maintaining an ultrasmall size (< 10 nm). Furthermore, they can be synthesized using non-heavy metals. Metal sulfides have been used in PA imaging [4,25,26,36], with copper sulfide (Cu_xS) previously demonstrated for PA imaging up to 5 cm [4]. However, Cu_xS has lower optical absorption compared with metallic nanoparticles (NPs), requiring higher doses for equivalent deep tissue imaging, increasing potential toxicity [5]. Improving PA signal generation within this class of materials could lower the dose required for effective imaging and further reduce concerns of dose-dependent toxicity.

Copper iron sulfides have large infrared LSPRs at ultrasmall sizes due to p-type doping [6,35,37,38]. Lee et al. described the emergence of pronounced NIR-II LSPR in colloidal chalcopyrite ($CuFeS_2$) and bornite (Cu_5FeS_4) compositions of copper iron sulfide when the NPs undergo oxidation-induced Fe leaching upon exposure to air. Analogous to binary copper sulfide nanocrystals, the decreased Fe content leaves metal vacancies in the nanocrystal lattice; charge-compensating holes resonate, generating the high optical absorbance seen in the NIR-II [35]. A recent transient absorption study by Kuszynski et al. demonstrates that in bornite, both the hole effective mass and hole density increase as Fe content decreases, thereby increasing carrier-mediated thermal conductivity [39]. This material characteristic likely contributes to contrast in photoacoustic imaging and heating efficiency in photothermal therapy. In this work, we evaluated bornite (Cu_5FeS_4) as a potential NIR-II PA imaging contrast agent. These particles have ultrasmall sizes (2.7–6.1 nm) with sharp LSPR in the NIR-II window, controlled by particle oxidation (iron leaching) [6]. Due to the small size, tunability, and potential biocompatibility of a material comprised of bioessential elements, we tested bornite as a photoacoustic contrast agent in phantoms and *in vivo*. Bornite demonstrated minimal toxicity in HepG2 liver cells. PA signal was detected at greater tissue depths from bornite NCs compared to conventional PA contrast agents. Finally, we demonstrated improved contrast from deeply embedded structures in mice at concentrations below toxicity levels.

2. Materials and methods

2.1. Contrast agents for photoacoustic imaging

Bornite NCs were synthesized following the protocol developed by Kays et. al. [6]. Briefly, a mixture of copper (II) acetylacetonate (Cu (acac)$_2$, ≥99.9 %, Sigma-Aldrich) and iron (III) acetylacetonate (97 %, Sigma-Aldrich) at Cu/Fe molecular ratios of 5:1 with 0.5 mmol (130 mg) of Cu and 0.1 (35 mg) mmol of Fe was stirred in 6.65 mL oleic acid (OA, technical grade, 90 %, Sigma-Aldrich). The mixture was flushed with argon while heating to 150 °C to dissolve all metal salts, with subsequent heating to 180 °C. Simultaneously, a 0.2 M solution of sulfur (99.99 %, Sigma-Aldrich) in oleylamine (technical grade, 70 %, Sigma-Aldrich) was flushed with argon and heated to 90 °C. Once the temperature of the Cu/Fe mixture reached 180°C, 1.5 mL of 1-dodecane-thiol (≥98 %, Sigma-Aldrich) was injected, resulting in a color change. Immediately afterward, 10 mL of the sulfur in oleylamine solution was injected into the mixture; after 90 seconds the reaction was stopped by removing the heat. Copper sulfide particles ($Cu_{2-x}S$) were synthesized with a modified method from literature [40]. Specifically, 0.4 mmol (105 mg) Cu(acac)$_2$ were dissolved in 7 mL OA similarly, and then heated to 240 °C. 1 mL 0.2 M sulfur in oleylamine solution was bolus injected into the mixture, before 3 mL of oleylamine was subsequently injected for 60 seconds annealing until stopped by removing heat. After synthesis, nanoparticles were stored protected from light in an argon-filled glovebox. Before use, nanoparticles were precipitated using 1:3 mixture of hexane:ethanol and then centrifuged at 14,000 rcf for 5 minutes to remove excess ligands and precursors. For *in vivo* use, the bornite and $Cu_{2-x}S$ particles were encapsulated in micelles consisting of 1,2-distearoyl-sn-glycero-3-phosphoethanolamine-N-[methoxy(polyethylene glycol)-2000 (DSPE-PEG2k; Avanti Polar Lipids) as previously described [41].

For transmission electron microscopy (TEM) imaging of bornite and $Cu_{2-x}S$ particles, particles were drop cast on carbon-coated copper TEM grids and imaged on a JOEL 2100. Particle cation concentrations were determined with microwave plasma atomic emission spectroscopy (MP-AES, Agilent, MA) on nitric acid dissolved samples. TEM images of AuNRs were provided by the manufacturer. Solutions of varying mass concentrations were prepared to compare the PA signal generation of bornite with other conventional agents: ICG, AuNRs and $Cu_{2-x}S$. Dilutions of bornite (6 dilutions of 0.11–0.64 mg/mL) were prepared in octadecene (Sigma-Aldrich O806–25 ML). Solutions of ICG (TCI Chemicals I0535) were prepared in DI water yielding mass concentrations of 0.25–1 mg/mL (3.2×10^2 to 1.3×10^3 μM), where a stable absorption peak at 780 nm was observed (measured absorbance spectra for ICG at specified concentrations is provided as supplemental Figure S4). The AuNRs (Nanopartz CP12–10–1064) used in this study were PEGylated with a methyl group allowing for dilution in DI water (0.05–0.55 mg/mL).

2.2. Toxicity

HepG2 cells (ATCC) were used for cell viability assays. Cells were plated in 96-well plates with a cell density of 40,000 cells/well and allowed to adhere overnight. Particles of varying concentrations were added to the cells for a 24-hour incubation with n = 4 for replicates. A CellTiter-Glo cell viability assay (Promega, WI) was used to measure cell viability. After nanoparticle incubation, cells were washed with a phosphate-buffer (PBS) (pH 7.4) and treated with the cell viability assay mixture following the assay protocol. After a 10 min incubation, the bioluminescence was measured in a plate reader (Paradigm, Molecular Devices, CA) using a 250 ms exposure time.

2.3. Concentration dependence of PA signals

Optical characterization of ICG, bornite and $Cu_{2-x}S$ were performed

using a spectrometer (Jasco V-770 UV-Vis-NIR); the absorption spectra of AuNRs was provided by the manufacturer. The mass concentrations of all contrast agents at the optical peak were verified using a plate reader (SpectraMax i3x) prior to imaging (for particles with peak absorption at 1064 nm, a reference wavelength of 900 nm was used). For the imaging studies, the optical density of ICG at 780 nm was matched to that of AuNRs, $Cu_{2-x}S$ and bornite at 1064 nm. PA imaging of the contrast agents was performed using a prototype 3D PA tomography system, the TriTom (PhotoSound Technologies, Inc., Houston, TX, USA) [42], integrated with a nanosecond Q-switch pulsed laser (Opotek Benchtop Phocus HE, Carlsbad, CA, USA). The laser generates 5–7 ns optical pulses at a 10 Hz repetition rate with a tunable range of 690–950 nm and 1200–2400 nm with a minimum step size of 1 nm. A 1064 nm beam can be accessed through a residual port on the laser head. In the TriTom system, four optical fiber terminals are mounted to the outer side of the water bath at 90° and 45° to the vertical plane of the transducer array to illuminate the object of interest (Fig. 2a). A sample holder was attached to a stepper motor for mechanical rotation of the imaged target. The position of the holder can be adjusted in the elevation direction within the 3D imaging volume of 40 $\times$40 x 40 mm^3. Image reconstruction was

restricted to a 30 $\times$30 x 30 mm^3 volume with a resolution of 150 μm (x & y axes). The generated acoustic waves were detected using a 6 MHz arc transducer array with 96 channels for PA signal acquisition. Each volumetric image was acquired in 36 seconds. The water bath was filled with deionized and degassed water for acoustic coupling [43].

PA imaging was performed at the peak wavelength of each contrast agent, with the energy at the fiber bundle input measured with an external power meter (Ophir Technologies, West North Logan, UT, USA). The laser energy was 52 mJ and 40 mJ at 780 and 1064 nm, respectively. The solutions were placed in polyethylene tubes (0.89 ± 0.05 mm inner diameter, 101.6 mm length) attached along the circumference of a circular disc. This circular disc was mounted onto the rotating platform and immersed in the water bath maintained at a constant temperature of 25 °C. Light was delivered through a fused optical fiber with four outputs, each of dimensions 1 $\times$30 mm^2, distributed at locations along the wall of the imaging system (Fig. 2a) [42]. The rotation and subsequent volumetric data acquisition creates a uniform light distribution at a constant radius. The 3D image for each agent was collected five times (five complete revolutions) and processed. A modified back projection algorithm was used to reconstruct PA
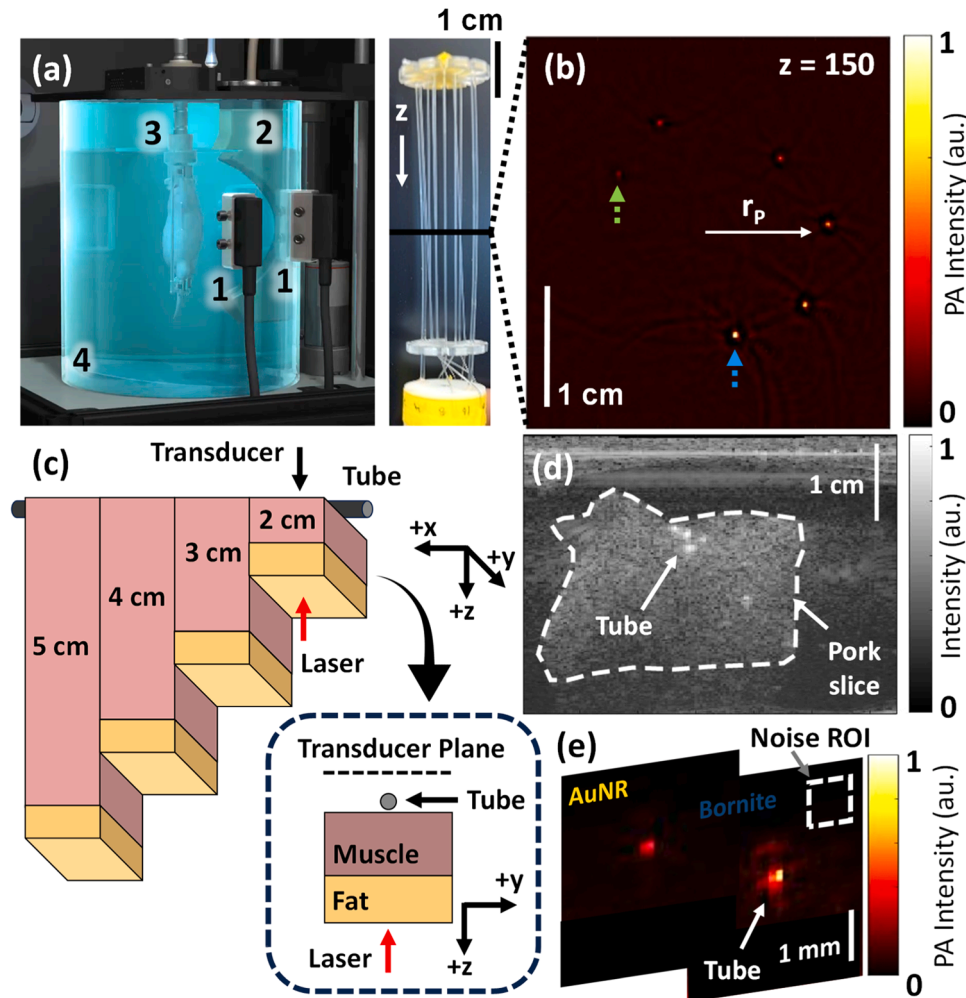

Fig. 2. PA imaging methods of bornite: (a-b) *3-D PA tomography of bornite using the TriTom.* (a) A photograph of the PA tomographic imaging system - 1) illumination ports, 2) ultrasound detection array, 3) animal or sample holder, 4) water tank. The solutions are placed along the circumference (with radius, r_p) of the phantom holder. (b) A representative PA image of the tube phantom carrying varying concentrations of bornite with the most (0.64 mg/mL) and least (0.11 mg/mL) concentrated solutions indicated with a blue and green arrow, respectively. (c-e) *2-D PA imaging of bornite in porcine tissue phantoms.* (c) Schematic representation of the phantom mold with individual tissue slices of varying depths - 2, 3, 4, 5 cm and a tube placed underneath. Optical illumination and acoustic detection are placed antiparallel to each other. The inset is a schematic of the orientation of the acquired images with arrows indicating the tube carrying the contrast agent, the optical illumination, and the acoustic detection. (d) A B-mode image of the 2 cm tissue slice (white dashes) with the cross-section of the tube (indicated with arrow). (e) 2-D PA images of the 2 cm tissue slice with the cross-section of the tube carrying AuNR and bornite. A ROI (white dashed box) describing an area of pixels corresponding to the noise is indicated.

images with a volume of 30 ×30 x 30 mm^3 [44]. The parameters required to reconstruct the 3D PA data included azimuthal and elevational angle of each transducer element to calculate solid angle, 3D array of photoacoustic data, speed of sound (SoS) and radial distance of transducer elements from the axis of rotation. The water heater used to maintain the temperature of the water bath produced significant noise in the acquired PA data. This required the heater to be turned off during data acquisition, resulting in a slight temperature drift. Image reconstruction precision was optimized by first reconstructing a 2D slice (z = 150) of the 3D image, orthogonal to the Tritom illumination port (labeled in Fig. 2a-b), at multiple SoS values (0.001 mm/μs step size). The SoS value which produced an undistorted image (the diameter of the reconstructed tube matched that of the physical tube) was used to reconstruct all images (1.426 mm/μs). Once reconstructed, the image signals were corrected for the wavelength-dependent absorption of water and laser fluence using Beer's law. The pixels of each tube containing the contrast agents were averaged within a 2D slice orthogonal to the Tritom illumination port (Fig. 2a-b) corresponding to the center of the excitation terminal (z = 150).

2.4. Assessment of maximum depth of ex vivo photoacoustic signal generation

Ex vivo porcine phantoms were prepared to assess the impact of tissue depth on photoacoustic signal generation from bornite and AuNRs. Porcine tissue was sliced into different thicknesses (2, 3, 4, 5 cm) and embedded into a gelatin mold (Fig. 2c). The gelatin mold was prepared at 10 % mass per volume with no other optical or acoustic attenuators. The sliced porcine tissue had two distinct layers – fat (0.3, 0.5, 1.2 & 1.9 cm) and muscle (1.7, 2.5, 2.8 & 3.1 cm). A clear polyvinyl chloride tube, with inner diameter of 2 mm and outer diameter of 3 mm, containing test solutions of 0.55 mg/mL (9 × 10^{-3} μM) AuNRs and 0.65 mg/mL (3.2 μM) bornite, corresponding to a peak OD of ~ 3 at 1064 nm, was positioned underneath the slices and sequentially imaged. Optical illumination and acoustic detection planes were perpendicular (Fig. 2c). A 0.5 cm diameter beam was used to irradiate the surface of porcine tissue with a uniform ~20 mJ/cm^2 fluence at 1064 nm.

An open architecture ultrasound data acquisition system (Vantage 256, Verasonics, Inc., Kirkland, WA, USA) was used to acquire the acoustic signals. The Vantage was coupled with a linear array 6 MHz (Bandwidth: 4–7 MHz) transducer (Philips L7–4, Amsterdam, Netherlands) and a front-end preamplifier (Photosound Legion Amplifier) that improved impedance matching and amplified low frequency signal detection by 40 dB. The q-switch of the laser was externally triggered by a function generator (AFG2021, Tektronix, OR, USA). All acquisition steps were controlled through a MATLAB 2018a (Mathworks, CA, USA) graphical user interface, while image reconstruction was performed using a standard delay-and-sum algorithm (key acquisition parameters are provided in the supplementary Table S2). The energy output of the laser was measured at the output port using a power meter (Ophir Technologies, West North Logan, UT, USA). Five PA images were averaged and used for further analysis.

Fig. 2(d) shows a B-mode image of the 2 cm slice of porcine tissue with the cross-section of the tube visualized. The reconstructed co-registered PA images are presented in Fig. 2e. Given the antiparallel optical illumination and acoustic detection, the acoustic path length remains the same across all porcine slices while the optical path length changes. A 3.5 mm × 3.5 mm area of pixels (15 × 15 pixels) encompassing the tube was selected from the B-mode image. The pixels within this area in the PA images were averaged to represent the total PA signal generated by the imaged contrast agent (I_{obj}). To calculate the average background noise (I_{Noise}) of the PA image, a region of pixels at the corner of the image was used (Fig. 2e). Contrast to noise ratio (CNR) was calculated using the following equation,

$$CNR = \frac{I_{obj} - I_{Noise}}{\sigma_{Noise}}$$

where σ_{Noise} is the standard deviation of the noise.

2.5. In-vivo assessment of bornite

The animal imaging protocol used in this study was approved by the Tulane University Institutional Animal Care and Use Committee (IACUC). Pregnant CD 1 mice at gestational day 16 were anesthetized with 1.5 % isoflurane mixed with 100 % oxygen at a flow rate of 1 L/min. The fur from the lower abdomen region, torso, and hind limb of the animal were removed by shaving followed by application of a depilatory cream. The limbs and tail of the animal were restrained to the animal holder with surgical tape. The animal was then placed in the imaging chamber and the torso of the animal was submerged in the deionized and degassed water bath, heated to maintain a body temperature of 37 °C. To ensure a constant flow of anesthesia to the mouse, the head of the mouse was placed inside a nose cone attached to the animal holder.

3D PA tomography images of the animals were acquired at 808 nm as an anatomical reference, followed by imaging at 1064 nm to match the wavelength of peak absorptions for both bornite and AuNRs. The bornite particles used for the *in vivo* injection were ~7 OD or 0.61 mg/mL (3.05 μM at 1064 nm) in a PBS solution, at a dose of 100 μL/30 g animal weight. This translates to a circulating concentration of ~0.026 mg/mL (0.13 μM) after dilution in the total blood volume of the animal. A separate solution of PEGylated AuNRs was also prepared in a PBS solution with peak OD matched (4.7 × 10^{-3} μM) to bornite. A catheter was surgically inserted into the jugular vein of the animal to deliver bolus injections of the prepared contrast agents and flushed with 100 μL of PBS. 3D images were collected pre-injection, post-injection and at ~1-minute intervals for the first 10 minutes, followed by 5-minute intervals, for a total duration of 60 minutes. Single timepoint 3D images were used for further analysis. Three unique anatomical regions – mammary arteries (2–5 mm from skin), ovarian arteries (9–12 mm from skin), and the placenta (3–10 mm from skin), were manually segmented. All 3D rendering and segmentation were performed using Amira (Thermo Fisher Scientific, MA, USA). The 3D PA images were normalized by the pre-injection image, and then the anatomy of interest was segmented. The pixels within each segmented ROI were averaged for further analysis. The sample sizes needed for statistical power were calculated using a MATLAB power analysis function (samplesizepwr) [45], and a sample size of 3 was determined to be sufficient to generate a power of 0.95. A one-way analysis of variance (ANOVA) was performed in MATLAB, followed by a post hoc t-test to differentiate the mean of the different groups.

3. Results

Dose dependent-biocompatibility of the PEGylated bornite NCs was assessed *in vitro* using the human liver cell line HepG2 and compared to Cu$_{2-x}$S particles (Fig. 3). Bornite showed a dose-dependent toxicity with high cell viability (> 90 %) up to a NP mass concentration of 0.06 mg/mL. A gradual decrease in cell viability was observed at increasing dose, with < 25 % cell viability at doses ~ 0.5 mg/mL. The bornite cell viability results were very similar to that measured for the Cu$_{2-x}$S particles, and these results are consistent with results seen in other copper sulfide cell viability studies [46–48].

Fig. 4 shows the optical characteristics of the four contrast agents. The PA signal generation of the four contrast agents (Bornite, ICG, Cu$_{2-x}$S & AuNRs) were characterized with the Tritom system (Fig. 5a). At similar mass concentrations, bornite NCs had a ~10x increase in generated PA signal compared to ICG & Cu$_{2-x}$S and a ~5x increase in generated PA signal compared to AuNRs. A linear regression of the measured PA signal as a function of the mass concentration was
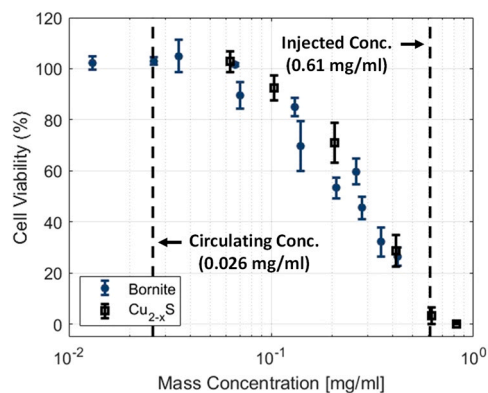
Fig. 3. In vitro toxicity of contrast agents. A quantitative analysis of the HepG2 cell viability after 24-hour treatment with bornite (blue solid circles) and $Cu_{2-x}S$ (black squares), respectively.
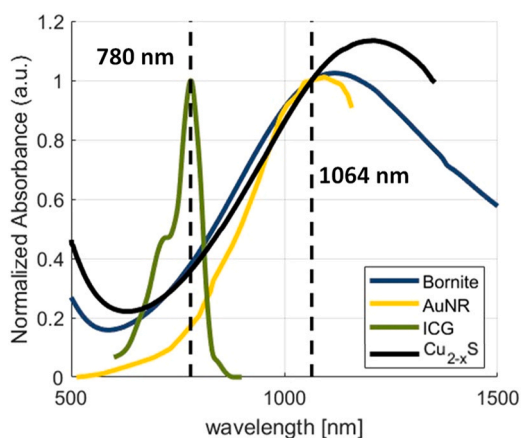

Fig. 4. Optical characterization of exogenous contrast agents: Absorbance spectra of the contrast agents – bornite (dark blue), AuNR (yellow), ICG (green) and $Cu_{2-x}S$ (black) at normalized mass concentrations. Wavelengths of experimental PA laser illumination indicated by dashed lines.

performed using MATLAB's linear regression toolbox (Fig. S1). A relatively linear response for all agents was observed.

Ex vivo porcine tissues were used to assess the maximum light depth at which a detectable PA signal was generated when imaging with bornite versus AuNRs. Fig. 5b shows the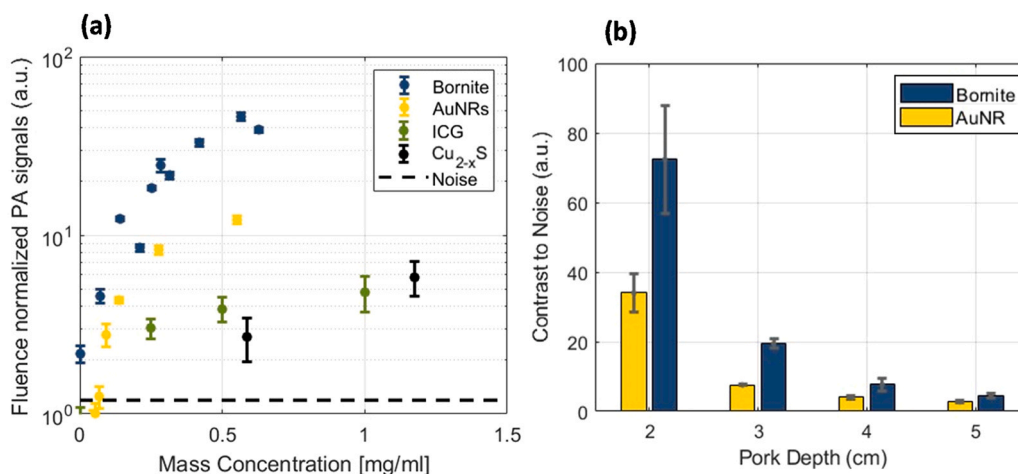 CNR of the two contrast agents as a function of imaging depth. Bornite showed a 2–3× increase in CNR at all imaging depths compared to AuNRs (Fig. 5b). A maximum imaging depth of 6.5 cm is estimated based on this ex vivo data (Figure S2).

Fig. 6a shows the PA image of the lower abdomen of mouse pre-injection (t = 0) acquired at 1064 nm. Fig. 6b and c show the resulting PA images of the lower mouse abdomen at maximum intensities of photoacoustic signal for bornite and AuNRs post-injection, respectively. The initial maximum intensities of bornite and AuNR were observed at 16- & 42-mins post injection, respectively. Fig. 6d summarizes the results of the *in vivo* biodistribution of bornite and AuNRs at various anatomical sites of the mice. A statistically significant 2x increase was observed in PA signals generated from the segmented arteries and placenta of mice injected with bornite versus those injected with AuNRs. For anatomical reference, PA images collected at 808 nm, before the intravenous injection of the desired contrast agent, are shown in the Supplement (Fig. S6).

4. Discussion

In this study, we demonstrate PA signal generation from bornite semiconductor plasmonic NCs, which strongly absorb in the NIR-II. Various biocompatible PA agents using organic constituents have been previously reported for NIR-II imaging [18–20]. Zhou et. al developed phosphorus phthalocyanines (P-Pc) with absorption at 1000 nm demonstrating imaging up to ~5 cm under a human arm [18]. However, the concentrations (~ 51 mg/mL) of P-Pc used to perform these studies are ~500x greater than the reported cytotoxicity thresholds [18]. In our study, bornite at concentrations at (or below) cytotoxic concentrations had a maximum imaging depth of ~6.5 cm under heterogeneous porcine tissue at 20 % of the ANSI limit for skin laser exposure (20 mJ/cm^2) [15].

Nanoparticle bioaccumulation is dependent on the size and shape of the nanoparticles [49–51]. The PEGylated bornite particles tested here were between 2 and 6 nm, which enabled rapid accumulation in comparison to traditional AuNR particles (16 mins for bornite vs. 42 mins for AuNRs, as shown in supplemental Figure S3). Bornite biocompatibility was comparable to $Cu_{2-x}S$ particles, as assessed via HepG2 cell viability. This is a promising first step for the biological application of bornite nanoparticles, given that copper sulfide has been favorably considered for photoacoustic imaging and photothermal therapy applications. Studies have noted that the low toxicity of Cu_xS is closely related to solubility limits that minimize the dissociation of excess free Cu ions [46]. A similar moderated ion dissociation and particle degradation is likely for bornite given the very similar composition to $Cu_{2-x}S$. AuNRs have limited renal clearance due to their size (~100 nm), rod-like shape,

Fig. 5. Photoacoustic imaging of bornite: (a) PA signal generated by the contrast agents as a function of the mass concentration of the sample. The dashed black line represents the noise floor of the imaging system. (b) Contrast to noise ratio of the two contrast agents as a function of porcine tissue depth.
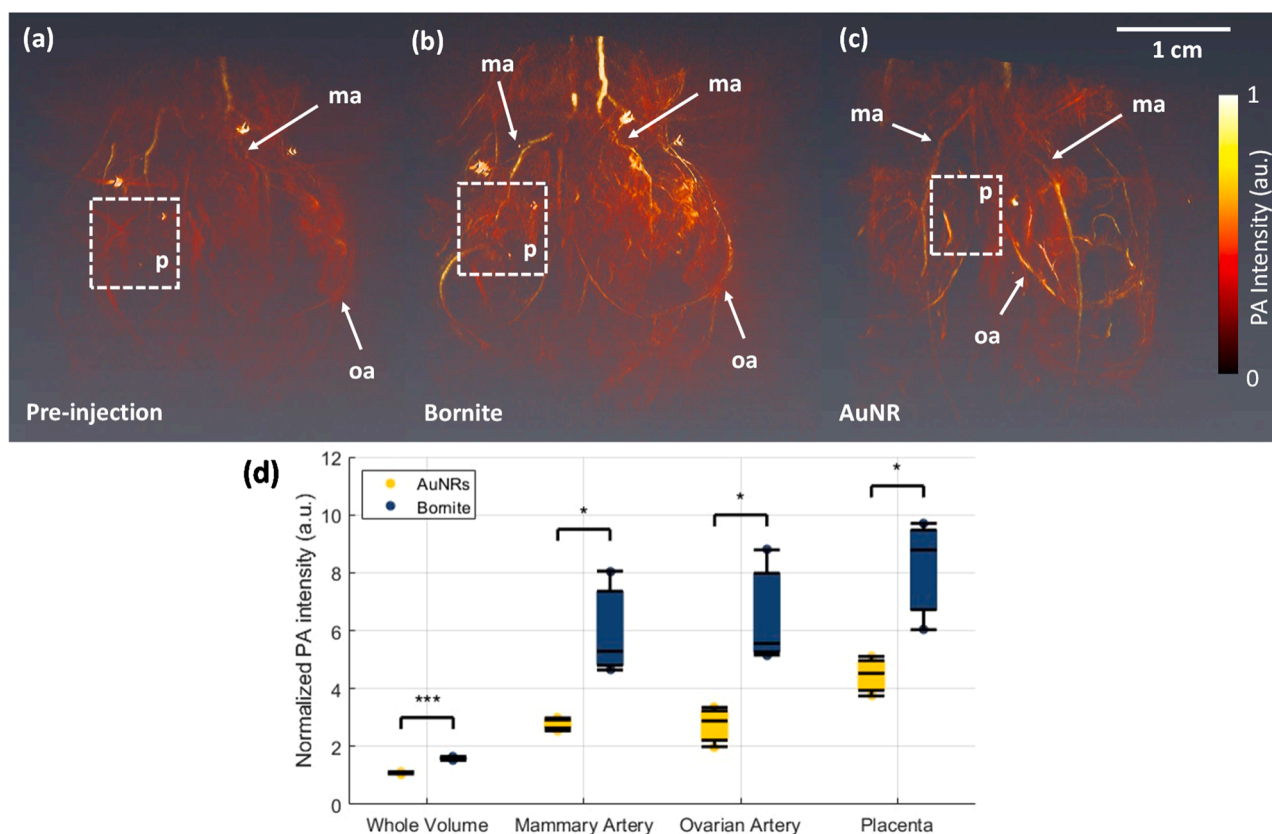
Fig. 6. In vivo characterization of bornite. (a) 3D PA image of a GD 16 lower mouse abdomen collected with the TriTom system prior to injection of contrast agent. 3D PA images of a GD 16 lower mouse abdomen injected with a ~7 OD solution of bornite (b) and AuNRs (c). The mammary arteries (ma), ovarian arteries (oa) and placenta (p) are indicated. (d) A box plot of pre-injection normalized PA signal from specific segmented anatomy – full reconstructed volume, mammary arteries, ovarian arteries, and placenta (n = 3 animals per group). A one-way analysis of variance (ANOVA) followed by a post-hoc t-test was performed to differentiate the means between bornite and AuNRs (p-values indicated using * - < 0.05 & *** - < 0.001).

and chemical inertness, which precludes degradation-mediated clearance [49]. In contrast, PEGylated Cu_xS particles (~30 nm diameter) have improved excretion in comparison to similar size and shape gold nanoparticles [52]. When directly compared, smaller (2.8 nm diameter) bovine serum albumin-coated copper sulfide nanoparticles were cleared more efficiently from rats than larger (18 nm diameter) particles, resulting in full recovery from transient and manageable hepatotoxicity, further indicating that smaller copper sulfide-based particles would be preferable for reduced bioaccumulation and increased biocompatibility *in vivo* [51]. Recently, Shi et. al. observed a thermosensitive degradation of nano-sized Cu_xS particles via thermal oxidation [53]. They noted that the nanoscale size of the particles allowed rapid degradation at low *in vivo* temperatures (37 °C) within one week. Size and compositional similarities to nominally biocompatible and excretable copper sulfide encourage further study of biomedical applications of bornite nanoparticles as an alternative to copper sulfide.

In our experiments, bornite generated PA signals up to depths of ~6.5 cm in porcine tissue phantoms. A consideration in the phantom experiments is that tissues demonstrate a frequency-dependent acoustic attenuation that will attenuate PA signals with a large acoustic path length. Due to challenges of coaxial alignment of the laser and transducer with our existing instrumentation, we were not able to reproducibly align our system in a parallel configuration, particularly for the larger imaging depths. In our study, we used a 6 MHz transducer (with a bandwidth of 4–7 MHz) to measure PA signals. The bandwidth of this transducer is band limited to lower frequencies that are minimally attenuated at larger acoustic pathlengths. Given that conventional clinical transducers for transabdominal imaging operate within these bandwidths, the utilization of bornite for deep vascular imaging

demonstrates significant potential.

The absorption cross-section of a colloidal nanostructure is directly related to the polarizability of the nanostructure [54]. At resonance excitation, an exponential polarizability is created due to a negative nanostructure permittivity. In metallic nanostructures, such as gold nanospheres, the high density of free charge carriers enables this negative permittivity resulting in strong resonant absorption peaks. In the case of plasmonic semiconductor materials, such as bornite, the permittivity is complex, including electronic effects (from interband or intraband excitation), atomic effects (from vibrational or phonon excitation), or conduction hole or electron excitations. The collective contribution of these effects can give rise to negative real permittivity resulting in strong optical absorption for semiconductor NPs [22,54]. Despite copper sulfide and bornite particles being well matched in size, concentration, and LSPR-based NIR-II absorption intensity, the bornite particles exhibit a 10-fold higher PA signal than the copper sulfide particles. Bornite has a similar or slightly higher carrier concentrations ($n = 10.6 \times 10^{21}$ cm^{-3} [6]), in comparison to copper sulfide, and substantially higher effective hole mass (1.28 m_e for bornite [6,39] vs 0.8 m_e for $Cu_{2-x}S$ [55]). Both the increased carrier concentration and effective hole mass contribute to increased thermal conductivity, which may lead to our observed increase in PA signal generation of bornite versus $Cu_{2-x}S$. The bornite particles exhibited a 5-fold increased PA signal compared to OD-matched AuNRs. While literature values for gold indicate similar or slightly higher carrier density and somewhat lower effective masses compared to bornite, the substantial difference in size between the bornite nanoparticles (~5 nm diameter) and AuNRs (~10 by 67 nm) leads to a large difference in the surface to volume ratio for the two particle types. This can lead to a greater PA pressure amplitude from

suspension of ultrasmall NCs with higher concentration under a nanosecond pulsed irradiation (a tabulated summary of physical and chemical properties of the different contrast agents can be found in supplemental Table S1).

Additionally, a suspension of ultrasmall bornite particles irradiated by a pulsed nanosecond laser generates more PA signal than larger rod-shaped AuNRs. Recently, Shahbazi and colleagues modeled the PA signal generation from core-shell gold nanospheres [56]. They reported that for a suspension of nanospheres, the PA signal drops superlinearly as the particle size increases. For a fixed concentration, the number of spheres in the suspension is inversely proportional to the sphere volume. This results in ultrasmall spheres generating larger PA signals due to the higher number density in suspension. In our study, a 0.1 mL solution of bornite will have an estimated 2.4×10^{19} particles in suspension while a solution of AuNRs of the same volume will only have approximately 1.8×10^{16} particles, potentially explaining the increased PA signal generation of bornite.

5. Conclusions

In conclusion, we have characterized bornite, a copper iron sulfide NC, as a NIR-II contrast agent for deep tissue photoacoustic imaging. The high NIR-II LSPR, ultrasmall size, and potential biocompatibility makes bornite an ideal candidate for imaging deeply embedded anatomy in *in vivo* applications. At similar mass concentrations, bornite had a $5\times$ improvement in PA signal generation when compared to AuNRs and a $10\times$ improvement when compared to ICG & $Cu_{2-x}S$. In porcine phantoms, a ~3 OD solution of bornite demonstrated a $2\times$ increase in image contrast compared to AuNRs at a light depth of 5 cm. An *in vivo* administration of PEGylated-bornite, at concentrations below toxicity, resulted in a $2\times$ improvement in pre-injection normalized PA signal generation from deeply embedded vasculature (such as the ovarian arteries), when compared to AuNRs. A similar, $2–3\times$ increase in CNR from bornite-injected anatomy was also observed. The results of this study demonstrate bornite as a biocompatible PA contrast agent for deep tissue imaging (up to depths of 6.5 cm). This opens the prospects of using PA imaging for deeper tissue imaging and targeting imaging using functionalized PEG for the conjugation of targeting moieties.

CRediT authorship contribution statement

Vinoin Devpaul Vincely: Data Curation, Formal analysis, Investigation, Methodology, Validation, Visualization, Witing - original draft, review & editing. **Xingjian Zhong:** Particle Synthesis, Writing - reviewing & editing. **Kristie Huda:** In vivo data collection, Writing - reviewing. **Swathi P. Katakam:** Phantom preparation, wiriting - reviewing. **Joshua C. Kays:** Preliminary Particle Synthesis, Writing - reviewing. **Allison M. Dennis:** Supervision, Resources, Project administration, Methodology. Wiritng - reviewing & editing. **Carolyn L. Bayer:** Supervision, Resources, Project administration, Methodology, Conceptualization, Funding Acquisition, Wiritng - reviewing & editing.

Declaration of Competing Interest

The TriTom system and Legion Amp were provided at no cost for evaluation. Carolyn Bayer reports financial support was provided by National Institutes of Health. Carolyn Bayer reports financial support was provided by The Chan Zuckerberg Initiative. Allison Dennis reports financial support was provided by National Institutes of Health. Allison Dennis reports financial support was provided by The Chan Zuckerberg Initiative. The other authors declare that they have no known competing financial interests or personal relationships that could have appeared to influence the work reported in this paper.

Data Availability

Data will be made available on request.

Appendix A. Supporting information

Supplementary data associated with this article can be found in the online version at doi:10.1016/j.pacs.2024.100649.

References

[1] J.V. Jokerst, A.J. Cole, D. Van de Sompel, S.S. Gambhir, Gold nanorods for ovarian cancer detection with photoacoustic imaging and resection guidance via Raman imaging in living mice, ACS Nano 6 (11) (2012) 10366–10377.
[2] Y.S. Chen, Y. Zhao, S.J. Yoon, S.S. Gambhir, S. Emelianov, Miniature gold nanorods for photoacoustic molecular imaging in the second near-infrared optical window, Nat. Nanotechnol. 14 (5) (2019) 465–472.
[3] Y.S. Chen, W. Frey, S. Kim, P. Kruizinga, K. Homan, S. Emelianov, Silica-coated gold nanorods as photoacoustic signal nanoamplifiers, Nano Lett. 11 (2) (2011) 348–354.
[4] G. Ku, M. Zhou, S.L. Song, Q. Huang, J. Hazle, C. Li, Copper sulfide nanoparticles as a new class of photoacoustic contrast agent for deep tissue imaging at 1064 nm, ACS Nano 6 (8) (2012) 7489–7496.
[5] A.N. Nikam, A. Pandey, G. Fernandes, S. Kulkarni, S.P. Mutalik, B.S. Padya, S. D. George, S. Mutalik, Copper sulphide based heterogeneous nanoplatforms for multimodal therapy and imaging of cancer: Recent advances and toxicological perspectives, Coord. Chem. Rev. 419 (2020).
[6] J.C. Kays, C.R. Conti, A. Margaronis, J.E. Kuszynski, G.F. Strouse, A.M. Dennis, Controlled synthesis and exploration of CuxFeS4 bornite nanocrystals, Chem. Mater. 33 (18) (2021) 7408–7416.
[7] Y. Mantri, J.V. Jokerst, Engineering plasmonic nanoparticles for enhanced photoacoustic imaging, ACS Nano 14 (8) (2020) 9408–9422.
[8] S. Singh, G. Giammanco, C.H. Hu, J. Bush, L.S. Cordova, D.J. Lawrence, J.L. Moran, P.V. Chitnis, R. Veneziano, Size-tunable ICG-based contrast agent platform for targeted near-infrared photoacoustic imaging, Photoacoustics 29 (2023).
[9] J. Weber, P.C. Beard, S.E. Bohndiek, Contrast agents for molecular photoacoustic imaging, Nat. Methods 13 (8) (2016) 639–650.
[10] C.L. Bayer, S.Y. Nam, Y.S. Chen, S.Y. Emelianov, Photoacoustic signal amplification through plasmonic nanoparticle aggregation, J. Biomed. Opt. 18 (1) (2013).
[11] Y.S. Chen, W. Frey, S. Aglyamov, S. Emelianov, Environment-Dependent Generation of Photoacoustic Waves from Plasmonic Nanoparticles, Small 8 (1) (2012) 47–52.
[12] S. Mallidi, T. Larson, J. Tam, P.P. Joshi, A. Karpiouk, K. Sokolov, S. Emelianov, Multiwavelength photoacoustic imaging and plasmon resonance coupling of gold nanoparticles for selective detection of cancer, Nano Lett. 9 (8) (2009) 2825–2831.
[13] C.A. Wood, S. Han, C.S. Kim, Y.F. Wen, D.R.T. Sampaio, J.T. Harris, K.A. Homan, J. L. Swain, S.Y. Emelianov, A.K. Sood, J.R. Cook, K.V. Sokolov, R.R. Bouchard, Clinically translatable quantitative molecular photoacoustic imaging with liposome-encapsulated ICG J-aggregates, Nat. Commun. 12 (1) (2021).
[14] L.D.B. Manuel, V.D. Vincely, C.L. Bayer, K.M. McPeak, Monodisperse Sub-100 nm Au nanoshells for low-fluence deep-tissue photoacoustic imaging, Nano Lett. 23 (16) (2023) 7334–7340.
[15] P.K. Upputuri, M. Pramanik, Photoacoustic imaging in the second near-infrared window: a review, J. Biomed. Opt. 24 (4) (2019).
[16] Z. Li, C. Zhang, X. Zhang, J. Sui, L. Jin, L. Lin, Q. Fu, H. Lin, J. Song, NIR-II functional materials for photoacoustic theranostics, Bioconjugate Chem. 33 (1) (2022) 67–86.
[17] S. Han, D. Lee, S. Kim, H.H. Kim, S. Jeong, J. Kim, Contrast agents for photoacoustic imaging: a review focusing on the wavelength range, Biosens. -Basel 12 (8) (2022).
[18] Y. Zhou, D. Wang, Y. Zhang, U. Chitgupi, J. Geng, Y. Wang, Y. Zhang, T.R. Cook, J. Xia, J.F. Lovell, A phosphorus phthalocyanine formulation with intense absorbance at 1000 nm for deep optical imaging, Theranostics 6 (5) (2016) 688–697.
[19] U. Chitgupi, N. Nyayapathi, J. Kim, D. Wang, B. Sun, C. Li, K. Carter, W.C. Huang, C. Kim, J. Xia, J.F. Lovell, Surfactant-stripped micelles for NIR-II photoacoustic

imaging through 12 cm of breast tissue and whole human breasts, Adv. Mater. 31 (40) (2019) e1902279.

[20] B. Park, K.M. Lee, S. Park, M. Yun, H.J. Choi, J. Kim, C. Lee, H. Kim, C. Kim, Deep tissue photoacoustic imaging of nickel(II) dithiolene-containing polymeric nanoparticles in the second near-infrared window, Theranostics 10 (6) (2020) 2509–2521.

[21] N. Beziere, N. Lozano, A. Nunes, J. Salichs, D. Queiros, K. Kostarelos, V. Ntziachristos, Dynamic imaging of PEGylated indocyanine green (ICG) liposomes within the tumor microenvironment using multi-spectral optoacoustic tomography (MSOT), Biomaterials 37 (2015) 415–424.

[22] A. Agrawal, S.H. Cho, O. Zandi, S. Ghosh, R.W. Johns, D.J. Milliron, Localized surface plasmon resonance in semiconductor nanocrystals, Chem. Rev. 118 (6) (2018) 3121–3207.

[23] L. Chen, H. Hu, Y. Chen, J. Gao, G. Li, Plasmonic Cu2−xS nanoparticles: a brief introduction of optical properties and applications, Mater. Adv. 2 (3) (2021) 907–926.

[24] X. Liu, M.T. Swihart, Heavily-doped colloidal semiconductor and metal oxide nanocrystals: an emerging new class of plasmonic nanomaterials, Chem. Soc. Rev. 43 (11) (2014) 3908–3920.

[25] D.Y. Santiesteban, D.S. Dumani, D. Profili, S.Y. Emelianov, Copper sulfide perfluorocarbon nanodroplets as clinically relevant photoacoustic/ultrasound imaging agents, Nano Lett. 17 (10) (2017) 5984–5989.

[26] S.H. Wang, A. Riedinger, H.B. Li, C.H. Fu, H.Y. Liu, L.L. Li, T.L. Liu, L.F. Tan, M. J. Barthel, G. Pugliese, F. De Donato, M.S. D'Abbusco, X.W. Meng, L. Manna, H. Meng, T. Pellegrino, Plasmonic copper sulfide nanocrystals exhibiting near-infrared photothermal and photodynamic therapeutic effects, ACS Nano 9 (2) (2015) 1788–1800.

[27] H.B. Cheng, Y.Y. Li, B.Z. Tang, J. Yoon, Assembly strategies of organic-based imaging agents for fluorescence and photoacoustic bioimaging applications, Chem. Soc. Rev. 49 (1) (2020) 21–31.

[28] J. Cao, T. Sun, K.T.V. Grattan, Gold nanorod-based localized surface plasmon resonance biosensors: a review, Sens. Actuators B: Chem. 195 (2014) 332–351.

[29] S. Link, M.A. El-Sayed, Shape and size dependence of radiative, non-radiative and photothermal properties of gold nanocrystals, Int. Rev. Phys. Chem. 19 (3) (2000) 409–453.

[30] J.B. Liu, M.X. Yu, C. Zhou, J. Zheng, Renal clearable inorganic nanoparticles: a new frontier of bionanotechnology, Mater. Today 16 (12) (2013) 477–486.

[31] M. Longmire, P.L. Choyke, H. Kobayashi, Clearance properties of nano-sized particles and molecules as imaging agents: considerations and caveats, Nanomedicine 3 (5) (2008) 703–717.

[32] R.D. Mellor, I.F. Uchegbu, Ultrasmall-in-nano: why size matters, Nanomaterials 12 (14) (2022).

[33] M. Semmler-Behnke, W.G. Kreyling, J. Lipka, S. Fertsch, A. Wenk, S. Takenaka, G. Schmid, W. Brandau, Biodistribution of 1.4-and 18-nm gold particles in rats, Small 4 (12) (2008) 2108–2111.

[34] S.M. Mousavi, S.A. Hashemi, S. Mazraedoost, K. Yousefi, A. Gholami, G. Behbudi, S. Ramakrishna, N. Omidifar, A. Alizadeh, W.H. Chiang, Multifunctional gold nanorod for therapeutic applications and pharmaceutical delivery considering cellular metabolic responses, oxidative stress and cellular longevity, Nanomaterials 11 (7) (2021).

[35] S. Lee, S. Ghosh, C.E. Hoyer, H. Liu, X. Li, V.C. Holmberg, Iron-content-dependent, quasi-static dielectric resonances and oxidative transitions in bornite and chalcopyrite copper iron sulfide nanocrystals, Chem. Mater. 33 (5) (2021) 1821–1831.

[36] Y.B. Li, W. Lu, Q.A. Huang, M.A. Huang, C. Li, W. Chen, Copper sulfide nanoparticles for photothermal ablation of tumor cells, Nanomedicine 5 (8) (2010) 1161–1171.

[37] L. Yuan, W.W. Hu, H. Zhang, L. Chen, J.Y. Wang, Q. Wang, Cu5FeS4 nanoparticles with tunable plasmon resonances for efficient photothermal therapy of cancers, Front. Bioeng. Biotechnol. 8 (2020).

[38] J.E. Kuszynski, J.C. Kays, C.R. Conti III, S.A. McGill, A.M. Dennis, G.F. Strouse, Effective mass for holes in paramagnetic, plasmonic Cu5FeS4 semiconductor Nanocrystals, J. Phys. Chem. C. 126 (30) (2022) 12669–12679.

[39] Jason E. Kuszynski, Xingjian Zhong, Stephen A. McGill, Allison M. Dennis, G. F. Strouse, Iron intermediate band governs relaxation kinetics of bornite plasmonic semiconductor nanocrystals, ACS Mater. Lett. (2024).

[40] X. Liu, X. Wang, B. Zhou, W.-C. Law, A.N. Cartwright, M.T. Swihart, Size-controlled synthesis of Cu2-xE (E = S, Se) nanocrystals with strong tunable near-infrared localized surface plasmon resonance and high conductivity in thin films, Adv. Funct. Mater. 23 (10) (2013) 1256–1264.

[41] A.M. Saeboe, J.C. Kays, A.M. Dennis, Encapsulating quantum dots in lipid-PEG micelles and subsequent copper-free click chemistry bioconjugation, Methods Mol. Biol. 2135 (2020) 95–108.

[42] W.R. Thompson, H.-P.F. Brecht, V. Ivanov, A.M. Yu, D.S. Dumani, D.J. Lawrence, S. Y. Emelianov, S.A. Ermilov, Characterizing a photoacoustic and fluorescence imaging platform for preclinical murine longitudinal studies, J. Biomed. Opt. 28 (3) (2023) 036001.

[43] K. Huda, C.X. Wu, J.G. Sider, C.L. Bayer, Spherical-view photoacoustic tomography for monitoring in vivo placental function, Photoacoustics 20 (2020).

[44] X. Minghua, L.V. Wang, Time-domain reconstruction for thermoacoustic tomography in a spherical geometry, IEEE Trans. Med. Imaging 21 (7) (2002) 814–822.

[45] MATLAB, sampsizepwr, (2006).

[46] W. Feng, W. Nie, Y. Cheng, X. Zhou, L. Chen, K. Qiu, Z. Chen, M. Zhu, C. He, In vitro and in vivo toxicity studies of copper sulfide nanoplates for potential photothermal applications, Nanomed.: Nanotechnol., Biol. Med. 11 (4) (2015) 901–912.

[47] X. Wan, M. Liu, M. Ma, D. Chen, N. Wu, L. Li, Z. Li, G. Lin, X. Wang, G. Xu, The ultrasmall biocompatible CuS@BSA nanoparticle and its photothermal effects, Front Pharm. 10 (2019) 141.

[48] K. Ding, J.F. Zeng, L.H. Jing, R.R. Qiao, C.Y. Liu, M.X. Jiao, Z. Li, M.Y. Gao, Aqueous synthesis of PEGylated copper sulfide nanoparticles for photoacoustic imaging of tumors, Nanoscale 7 (25) (2015) 11075–11081.

[49] Y.C. Wei, L. Quan, C. Zhou, Q.Q. Zhan, Factors relating to the biodistribution & clearance of nanoparticles & their effects on *in vivo* application, Nanomedicine 13 (12) (2018) 1495–1512.

[50] X.R. Song, N. Goswami, H.H. Yang, J.P. Xie, Functionalization of metal nanoclusters for biomedical applications, Analyst 141 (11) (2016) 3126–3140.

[51] Y.-N. Xia, H. Zu, H. Guo, T. Jiang, S. Yang, H. Yu, S. Zhang, H. Ding, X. Li, Y. Wang, Y. Wang, L.W. Zhang, Preclinical safety and hepatotoxicity evaluation of biomineralized copper sulfide nanoagents, J. Nanobiotechnol. 20 (1) (2022) 185.

[52] L. Guo, I. Panderi, D.D. Yan, K. Szulak, Y. Li, Y.-T. Chen, H. Ma, D.B. Niesen, N. Seeram, A. Ahmed, B. Yan, D. Pantazatos, W. Lu, A Comparative study of hollow copper sulfide nanoparticles and hollow gold nanospheres on degradability and toxicity, ACS Nano 7 (10) (2013) 8780–8793.

[53] S. Shi, X. Wen, T. Li, X. Wen, Q. Cao, X. Liu, Y. Liu, M.D. Pagel, C. Li, Thermosensitive biodegradable copper sulfide nanoparticles for real-time multispectral optoacoustic tomography, ACS Appl. Bio Mater. 2 (8) (2019) 3203–3211.

[54] Craig F. Bohren, D.R. Huffman, Particles small compared with the wavelength, Absorpt. Scatt. Light Small Part. (1998) 130–157.

[55] P. Lukashev, W.R.L. Lambrecht, T. Kotani, M. van Schilfgaarde, Electronic and crystal structure of Cu₂-ₓS: Full-potential electronic structure calculations, Phys. Rev. B 76 (19) (2007).

[56] K. Shahbazi, W. Frey, Y.S. Chen, S. Aglyamov, S. Emelianov, Photoacoustics of core-shell nanospheres using comprehensive modeling and analytical solution approach, Commun. Phys. 2 (2019).

Vinoin Devpaul Vincely received a B.S. in Biophysics and M. S. in Physics from Miami University in 2020. There he developed a fundamental knowledge of biophotonics working with Dr. Karthik Vishwanath. Currently, he is pursuing a Ph.D in Biomedical engineering from Tulane university as a part of the biomedical functional imaging laboratory, headed by Dr. Carolyn L. Bayer. His current research focus is to develop photoacoustic imaging systems for deep tissue quantitative imaging that address unmet clinical issues.

Xingjian Zhong is a Ph.D. candidate in the Department of Biomedical Engineering at Boston University. He received his B.S. degree in Biomedical Engineering from the Hong Kong Polytechnic University in 2019. He is currently conducting research at the Dennis lab in the Department of Chemical Engineering at Northeastern University. His research focuses on synthesizing NIR-II active quantum dots and nanoparticles for in vivo imaging applications and exploring the biodegradation and toxicity of copper chalcogenide nanocrystals.

Dr. Kristie Huda is currently a Research Scientist at G.E. HealthCare and received a Ph.D. degree in Biomedical Engineering at Tulane University in 2022. She completed her MS from University of Dhaka, Bangladesh in Biomedical Technology and Physics. Her research interests are medical imaging for women's health, simulation and modelling, and system development for clinical translation of imaging modality.
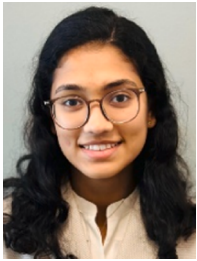
Swathi P. Katakam is currently a Master's student in electrical engineering at the University of Illinois Urbana-Champaign. She received her Bachelors in biomedical engineering from Tulane University. She is interested in investigating image processing techniques to improve the effectiveness of medical imaging tools.

Dr. Allison M. Dennis is currently an Associate Professor in Chemical Engineering and Bioengineering at Northeastern University after starting her independent career in Biomedical Engineering and Materials Science and Engineering at Boston University. She earned her PhD in Bioengineering at the Georgia Institute of Technology and conducted postdoctoral research in nanomaterials chemistry at the Center for Integrated Nanotechnologies at Los Alamos National Laboratory. Her research group develops optically active semiconductor nanoparticles for biomedical imaging and biosensing applications.
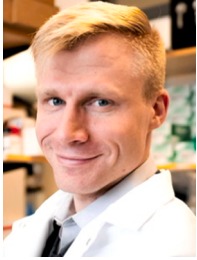
Dr. Joshua C. Kays received his Ph.D. degree from Boston University under the supervision of Dr. Allison Dennis. He is currently a faculty lecturer at Boston University. Joshua's primary research interests focus on Nanomedicine, Quantum Dots, Engineering Education, Translational Research, Biotechnology.

Dr. Carolyn L. Bayer obtained her Ph.D. degree from The University of Texas at Austin and is currently an Assoicate Professor in the Department of Biomedical Engineering at Tulane University in New Orleans, LA. Prior to joining Tulane University, Prof. Bayer was an NIH Ruth L. Kirschstein NRSA (F32) Postdoctoral Fellow at The University of Texas at Austin. Her research interests are in noninvasive imaging for assessment of placental function, diagnosis of pregnancy pathologies, and development of new therapies to treat diseases that lead to abnormal placental function and development.